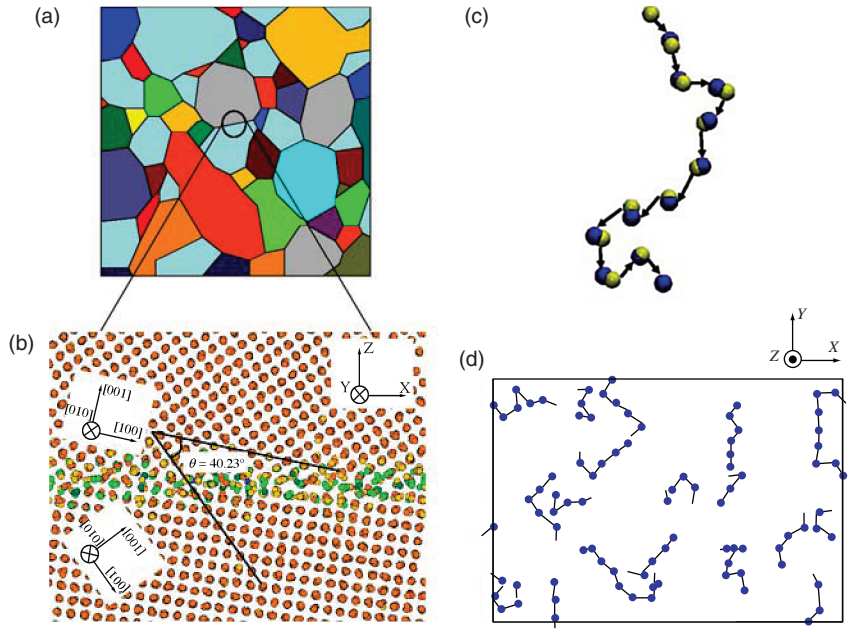

Figure 19.1. Illustration of string-like cooperative atomic motion within a GB. (**a**) Schematic microstructure of polycrystalline metal. Different colors indicate the individual grain having different orientations and the black line segments represent GB. (**b**) Equilibrium boundary structure projected onto the X–Z plane for $\theta = 40.23^\circ$ [010] general tilt boundary at $T = 900$K (X, Y, and Z-axes are Laboratory-fixed Cartesian coordinates, while [100], [010], and [001] refer to crystallographic axes). Upper and lower grains rotate relatively to each other by 40.23° along the common tilt axis [010]. The misorientation angle $\theta = 40.23^\circ$ does not correspond to a special Σ value (Σ refers to the ratio of the volume of coincidence site lattice to the volume of crystal lattice.). The atoms are colored by their coordination numbers q (orange: $q = 12$; others: $q < 12$). The simulation cell was chosen to have the grain boundary plane normal to the Z-axis. (c) Representative string within GB plane. Yellow and blue spheres represent the atoms at an initial time $t = 0$ and a later time, t^*. (d) Snapshot of string-like cooperative motion within the grain boundary region at $T = 900$K at $\Delta t = t^*$. The rectangular box illustrates the simulation cell in the X–Y plane. The application of a biaxial strain ε_{xx} and ε_{yy} in the X–Y plane (see inset) provides a driving force for GB migration that arises from the elastic energy difference between the grains. Figure 1 was originally published in Ref. [16], © National Academy of Sciences.

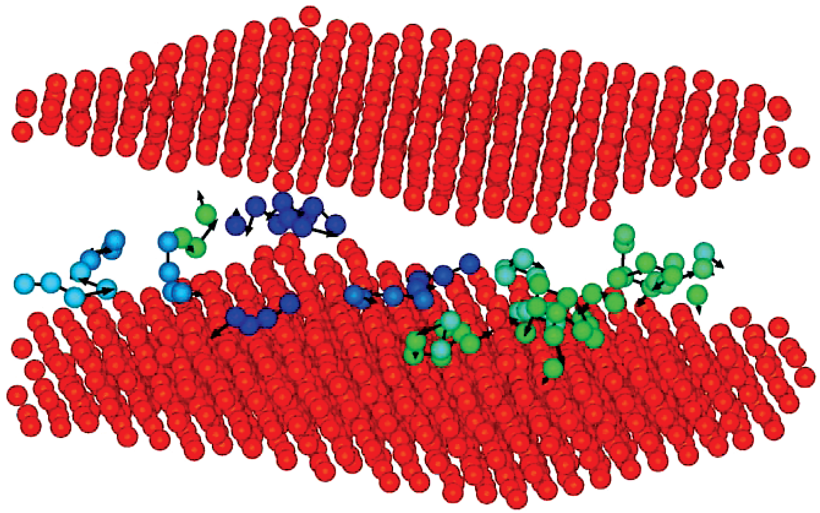

Figure 19.2. String-like cooperative motion within grain boundary region. The red atoms represent upper and lower crystal grains (displaced vertically to aid viewing) and the atoms with arrows indicate the atoms involved in the cooperative motion within a time interval Δt. Only strings having at least three atoms are shown; different colors indicate distinct strings.

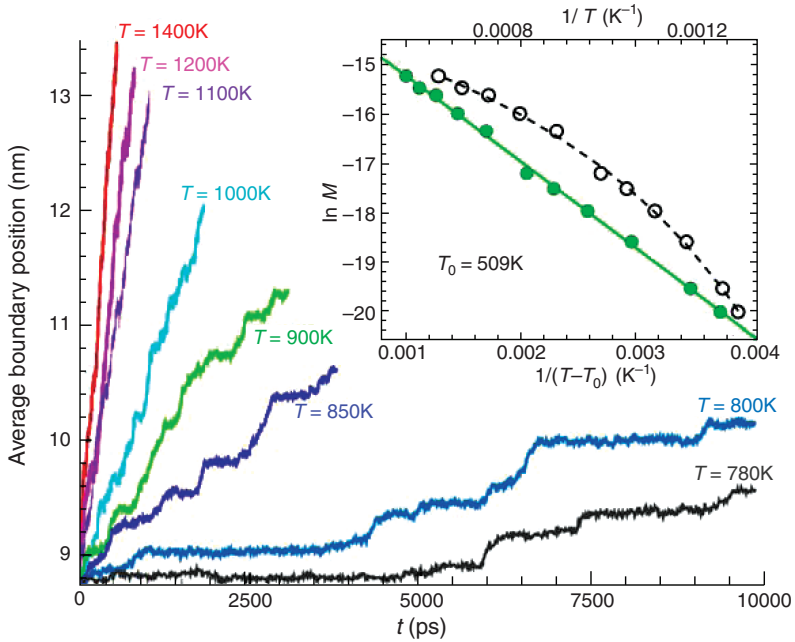

Figure 19.3. Temporal evolution of the average boundary position at eight different T. The inset shows the logarithm of the boundary mobility as a function of T [open circles versus $1/T$ (top axis) compare the data to an Arrhenius relationship, whereas the filled circles compare to the Vogel–Fulcher equation (bottom axis)]. The nonlinearity of the Arrhenius plot indicates that this relationship does not apply to GB mobility data. Figure 3 was originally published in [16], © National Academy of Sciences.

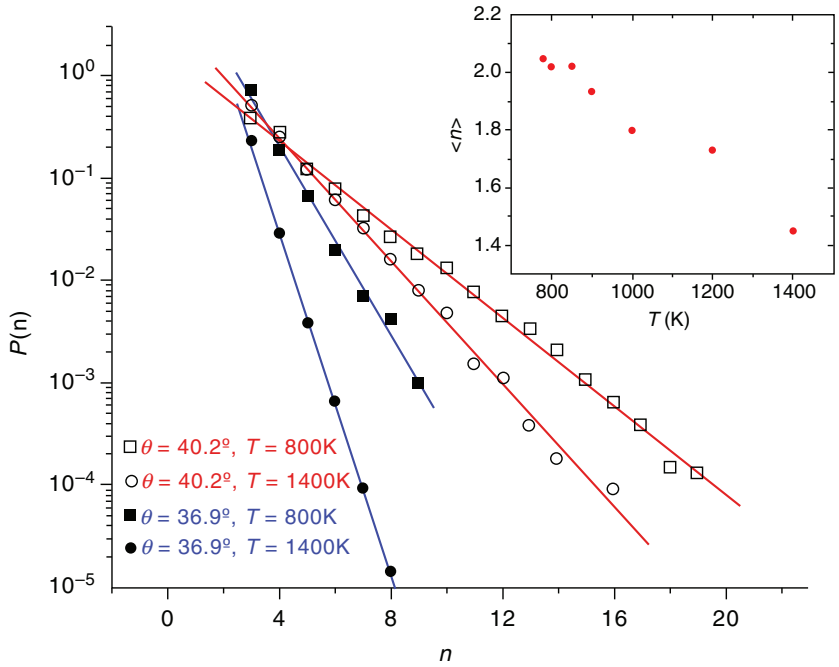

Figure 19.4. String length distribution function $P(n)$ for $\theta = 36.9^\circ$ boundary (Σ GB) and $\theta = 40{\cdot}2^\circ$ boundary (non-Σ GB) at 800K and 1400K, respectively. The inset shows the average string length $\langle n \rangle$ as a function of T for the GB, illustrating the growth of the scale of collective atomic motion upon cooling. The scale of $\langle n \rangle$ at a corresponding reduced temperature is similar to that of previous simulation observations on GF liquids [8,23]. Figure 4 was originally published in [16], © National Academy of Sciences.

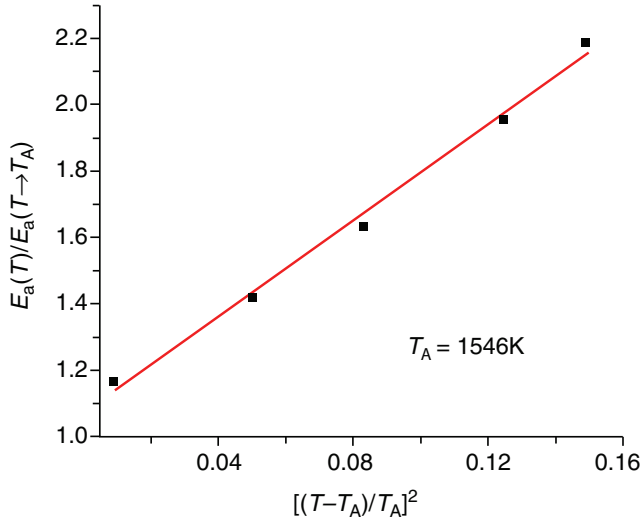

Figure 19.5. Reduced apparent activation energy, $E_a\,(T)\,/\,E_a\,(T \rightarrow T_A)$, for the grain-boundary mobility, $M(T)$, as a function of reduced temperature, $[(T - T_A)/T_A]^2$. This allows us to estimate the onset temperature for string-like cooperative motion, T_A.

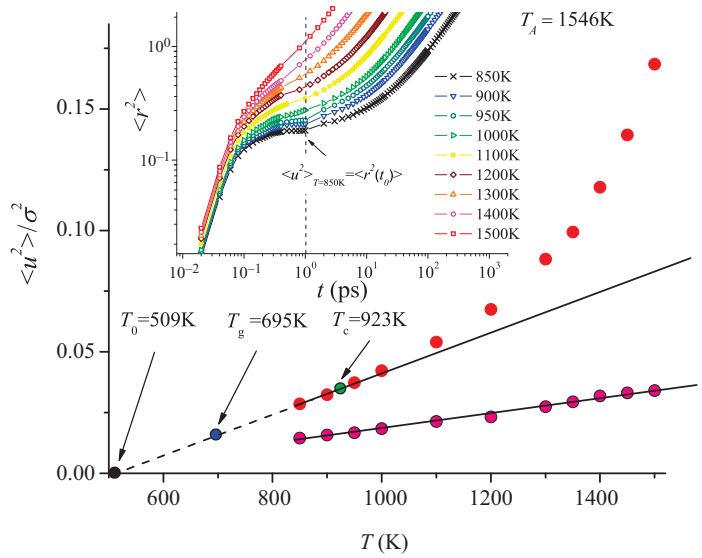

Figure 19.6. Debye–Waller factor $\langle u^2 \rangle$ as a function of T for the GB and crystal. The solid red circles represent the DWF for GB and the solid pink circles in the lower corner of the figure indicate the DWF for the lower grain. We observe that $\langle u^2 \rangle$ for the GB atomic motion (upper curve) is substantially larger than the scale of atomic motion in the grain (lower curve), $\langle u^2 \rangle$ in the grain only obtaining a value comparable to the Lindemann value for temperatures near $T_m = 1621$K [17]. The Vogel–Fulcher temperature T_0, determined from fitting the T dependence of boundary mobility data in Fig. 3, nearly coincides with the T at $\langle u^2 \rangle$ extrapolates to 0. $T_A = 1546$K approximates the onset of the supercooling regime and was also determined from the $M(T)$ data in Fig. 5. The crossover temperature T_c is determined from the GB fluid structural relaxation time (see Fig. 7) and T_g is estimated by the condition $\langle u^2 \rangle / \sigma^2 \approx 0.125$, where σ is the interatomic distance in the crystal, a Lindemann condition for glass formation [35]. All the characteristic temperatures estimates correspond to a relatively strong glass-forming liquid, as expected for metallic glasses. The inset shows the $\langle r^2(t) \rangle$ data from which $\langle u^2 \rangle \equiv \langle r^2(t_0) \rangle$ was determined. Vertical dotted line indicates the inertial decorrelation time, t_0 [32]. Figure 6 was originally published in [16], © National Academy of Sciences.

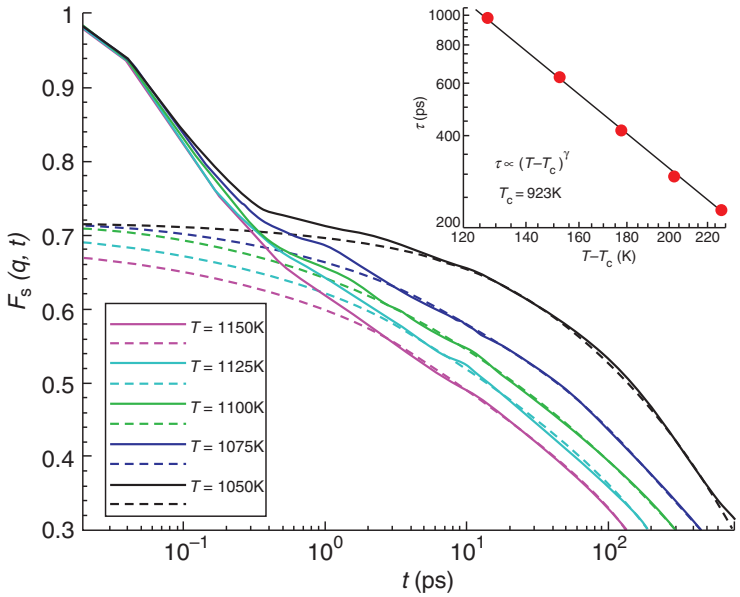

Figure 19.7. The self-intermediate scattering function for GB particles in the T range of 1050–1150K (defined in the text). The dashed curves are a fit of the stretched exponential relation, $F_s(q, t) \propto \exp\left[-(t/\tau)^\beta\right]$ to the long-time data, where the short-time decay arises from the inertial atomic dynamics. The inset shows a power fit of τ to $T - T_c$, where T_c and γ are adjustable parameters as in previous measurements and simulations. Figure 7 was originally published in [16], © National Academy of Sciences.

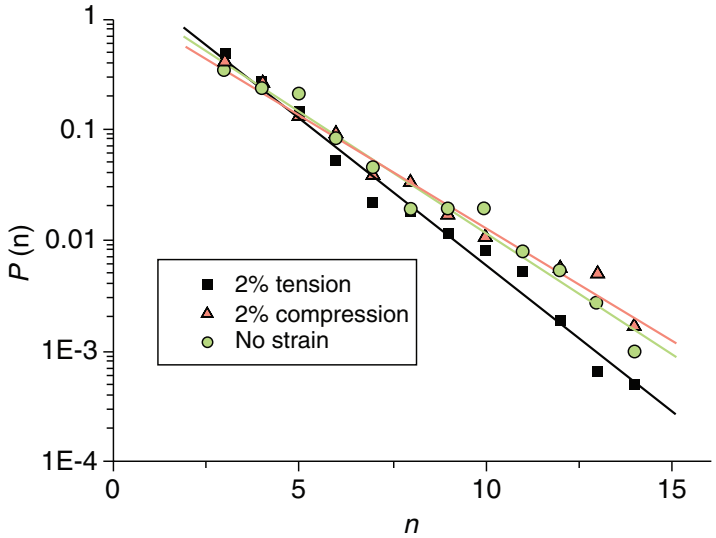

Figure 19.8. Effects of applied strain or pressure on the string length distribution function for a Σ5 [010] tilt grain boundary at 800K. In this study, the GB tilt axis was chosen to be oriented along the [010] axis, the tilt angle was taken to be $\theta = 36.8^{\circ}$ and one of the boundary planes is [001]. Under the strain conditions, that is $\varepsilon_0 = 0$ %, 2 %, and -2 %, the average string length $\langle n \rangle$ was found to equal 1.98, 1.63, and 2.13, respectively, where $\langle n \rangle$ is determined by the slopes of these curves, depends on the nature of the applied strain.

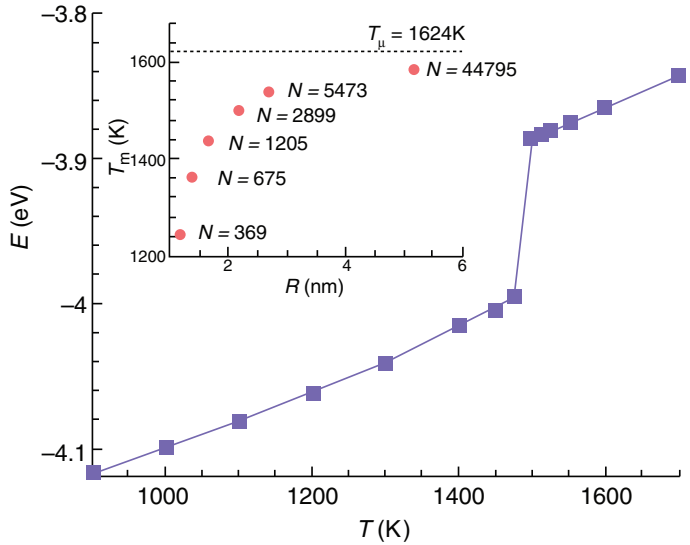

Figure 19.9. Determination of melting temperature T_{m} of Ni NP. The inset shows variation of T_{m} with the Ni NP size R. The radius of the NP is defined as $R = R_{\mathrm{g}}\sqrt{5/3} + R_{\mathrm{Ni}}$, where R_{g} is the radius of gyration $R_{\mathrm{g}}^2 = (1/N)\sum_i (R_i - R_{\mathrm{cm}})^2$ and $R_{\mathrm{N}i}$ is half the atomic distance in Ni bulk at the temperature of interest.

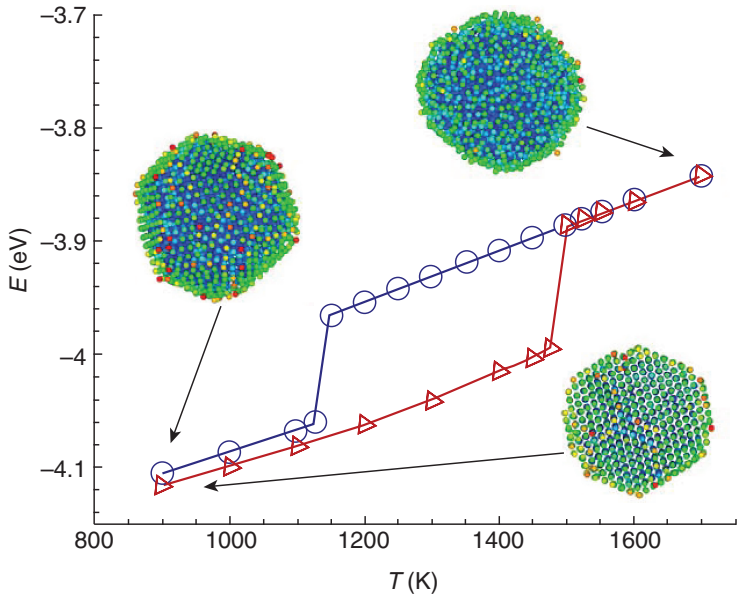

Figure 19.10. Potential energy per atom for heating and cooling cycles of an Ni cluster comprised 2899 Ni atoms. Figure 10 was originally published in [67], © American Chemical Society.

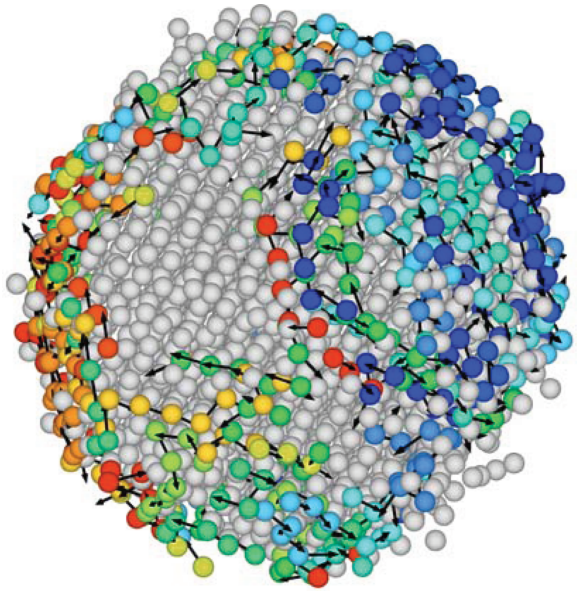

Figure 19.11. String-like collective atomic motion on the surface of Ni NP at equilibrium. The lines denote Ni atoms that belong to the same collective atom movement and the colors are introduced to help discriminate between distinct strings where $T = 1450$K; $N = 2899$; NP radius $= 2$ nm.

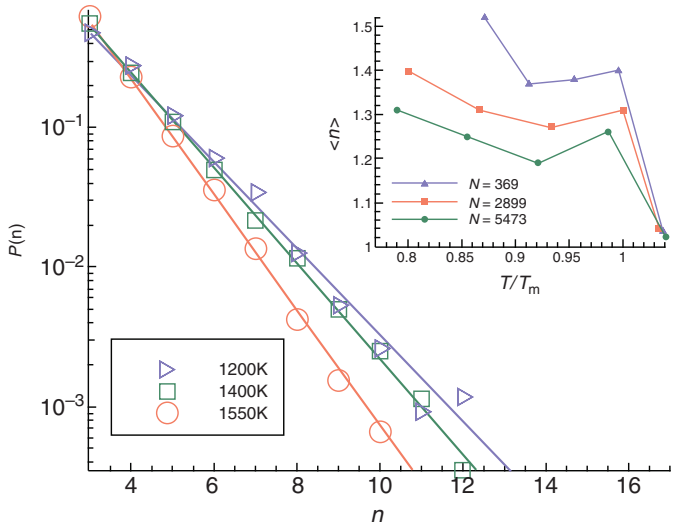

Figure 19.12. The size distribution and mean string length of the strings of interfacial collective motion as a function of reduced temperature T/T_m. The size of the particle corresponds to $N = 2899$. The inset shows the T dependence of the average string length $\langle n \rangle$ as a function of NP size. Figure 12 was originally published in [71], © Royal Society of Chemistry. In recent work we have refined this estimate of the temperature dependence and have used the maximum in the non-Gaussian parameter to define the strings. This new definition leads to the same qualitative trend that smaller particles have a stronger T dependence of $\langle n \rangle$, but there is no peak value of the string length as function of T as in the inset of Fig. 12. See [H. Zhang and J. F. Douglas, Soft Matter, 2012, DOI: 10.1039/C2SM26789F] for further discussion.

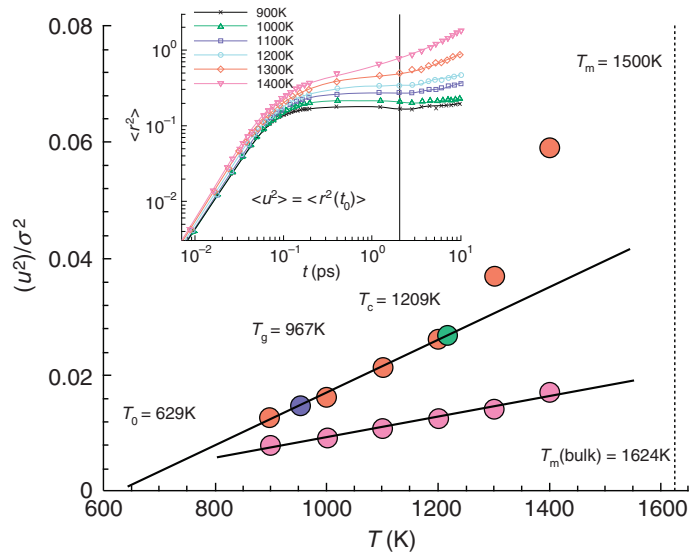

Figure 19.13. Average mean square particle displacement and Debye–Waller factor of interfacial and crystal core atomic motion of a Ni nanoparticle. Filled red circles denote the interfacial particles and the pink filled circles in the lower corner of the figure denote the crystal core particles. The size of the particle corresponds to $N = 2899$ atoms or a NP radius $= 2.0$ nm. Figure 13 was originally published in [71], © Royal Society of Chemistry.

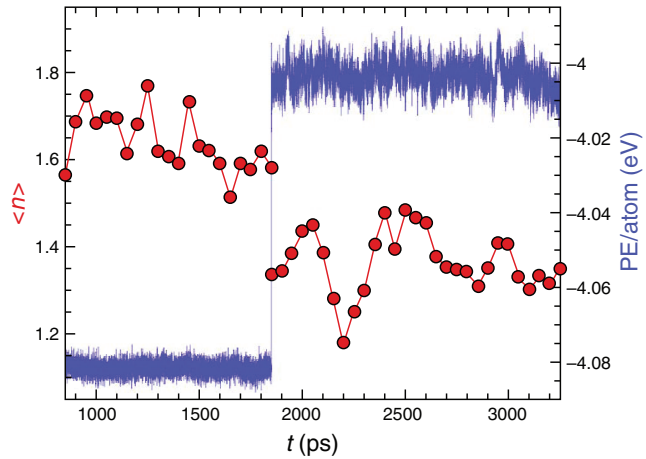

Figure 19.15. Evolution of the average string length $\langle n \rangle$ characterizing the interfacial atomic motions of an NP ($N = 2899$; radius $= 2$ nm) following an upward jump of the temperature to a new steady value below size-dependent T_{m} of the NP. Figure 15 was originally published in [71], © Royal Society of Chemistry.

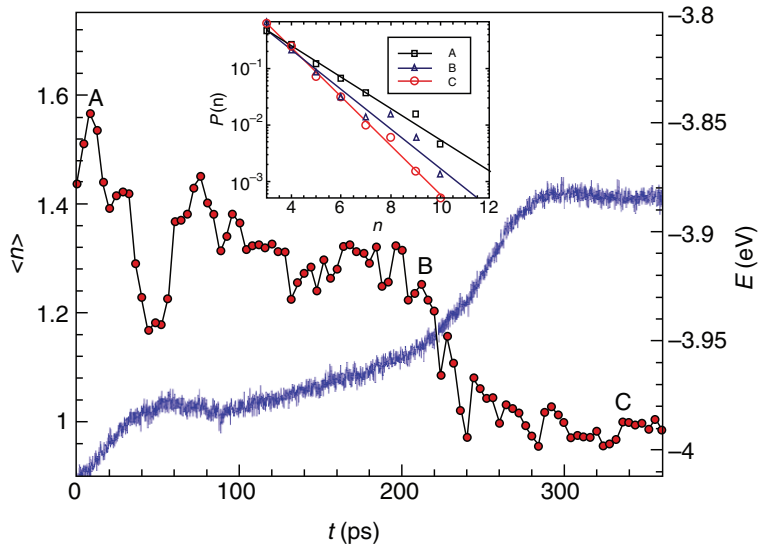

Figure 19.17. Evolution of the average string length $\langle n \rangle$ characterizing the interfacial atomic motions of an $N = 2899$ NP at $T = 1500$K. The inset shows the size distribution of the collective atom motions at the representative time points A, B, and C in the main plot.

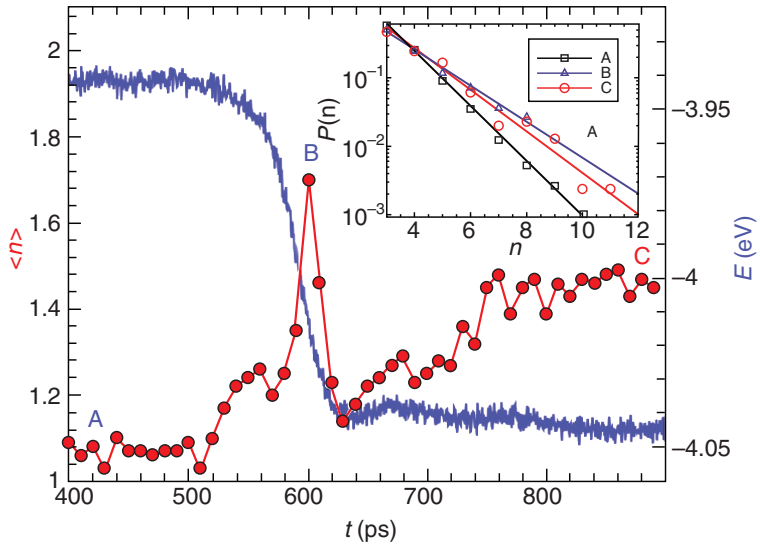

Figure 19.19. Evolution of the average string length $\langle n \rangle$ characterizing the interfacial atomic motions of an $N = 2899$ NP following a downward jump of the T to a new steady value. The inset shows the size distribution of the collective atom motions at the representative points A, B, and C in the main plot. Figure 19 was originally published in [67], © American Chemical Society.

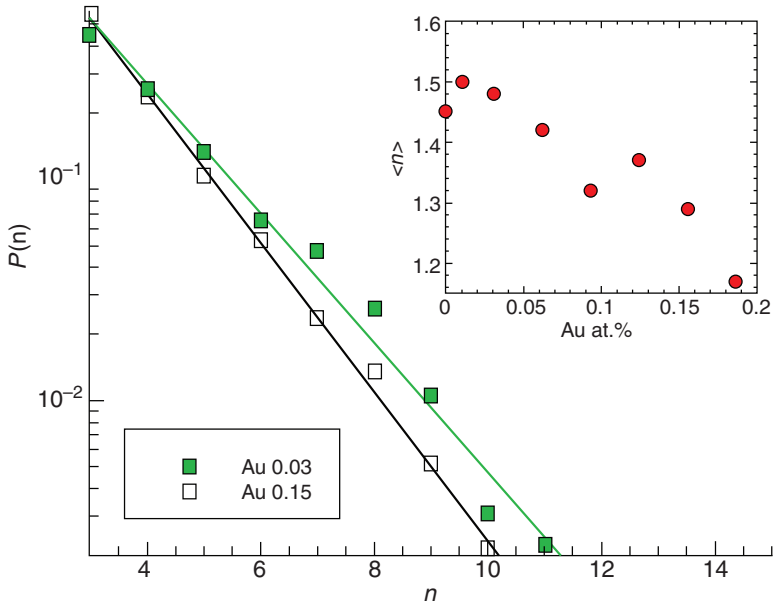

Figure 19.20. Change in string length in Ni nanoparticle ($N = 2899$; NP radius $= 2$ nm) interfacial region due to presence of Au impurities at $T = 900$K.

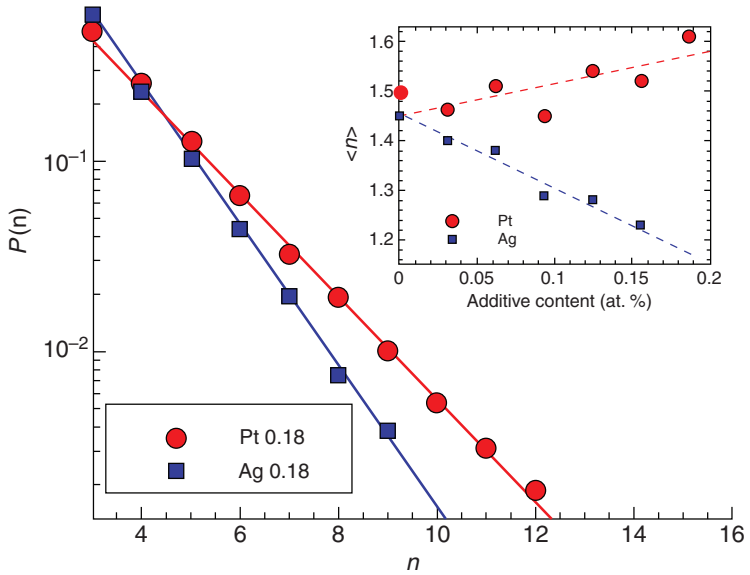

Figure 19.21. Change in string length in Ni NP($N = 2899$; NP radius $= 2$ nm) interfacial region due to Ag and Pt alloying at $T = 900$K with an 18% additive metal by relative mass. Dashed lines in the inset added to guide the eye. Figure 21 was originally published in [71], © Royal Society of Chemistry.